Fuel Cells

DOI: 10.1002/ange.201408845

Mapping Platinum Species in Polymer Electrolyte Fuel Cells by Spatially Resolved XAFS Techniques**

*Shinobu Takao, Oki Sekizawa, Shin-ichi Nagamatsu, Takuma Kaneko, Takashi Yamamoto, Gabor Samjeské, Kotaro Higashi, Kensaku Nagasawa, Takuya Tsuji, Motohiro Suzuki, Naomi Kawamura, Masaichiro Mizumaki, Tomoya Uruga, and Yasuhiro Iwasawa**

Abstract: *There is limited information on the mechanism for platinum oxidation and dissolution in Pt/C cathode catalyst layers of polymer electrolyte fuel cells (PEFCs) under the operating conditions though these issues should be uncovered for the development of next-generation PEFCs. Pt species in Pt/C cathode catalyst layers are mapped by a XAFS (X-ray absorption fine structure) method and by a quick-XAFS-(QXAFS) method. Information on the site-preferential oxidation and leaching of Pt cathode nanoparticles around the cathode boundary and the micro-crack in degraded PEFCs is provided, which is relevant to the origin and mechanism of PEFC degradation.*

The polymer electrolyte fuel cell (PEFC) is one of the clean energy-converting devices with high power density and efficiency, which brings low or even zero emissions into reality.[1] For wide-spread commercialization of PEFC vehicles, improvement of reliability and durability are indispensable. To meet these requirements, test and diagnosis methods are used to validate the membrane electrode assembly (MEA) catalyst designs and provide fundamental spatial information which is mandatory for the development of next-generation PEFCs. Particularly, it is necessary to clarify the key factors and mechanisms which promote or degrade catalytic activities of Pt/C cathode catalysts and improve their durability for oxygen reduction reactions (ORRs).[1b,2]

Catalyst characterization by, for example, NMR spectroscopy, Raman spectroscopy, FTIR/ATR-IR spectroscopy, TEM/SEM, XRD, neutron scattering, soft X-ray XPS, have been studied extensively,[3] but it is difficult to observe the dynamic and spatial behavior and transformation of Pt nanoparticles under the operating conditions of a PEFC. The in situ time-resolved X-ray absorption fine structure (XAFS) for PEFCs has recently been determined, the dynamic transformations of structures and electronic states of Pt/C and Pt_3Co/C cathode catalysts was elucidated, and elementary steps and their rate constants for the chemical events at the catalyst surfaces were determined, involving Pt valence change and Pt–O/Pt–Pt bond transformations.[4] These key reaction processes, which regulate the durability of PEFCs as well as the ORR activity, may occur in the space of the cathode layer because of the spatially heterogeneous properties and distribution of the Pt nanoparticles and carbon supports and the microscopically non-uniform potentials loaded in the cathode layer under PEFC potential operations.[5] The cathode degradation mechanism has also been studied to improve the MEA durability, which becomes a more serious issue.[6] Therefore, the nanoscopic spatial position and the mechanism of the dissolution and deterioration of the Pt/C cathode catalysts in MEAs should be uncovered to develop next-generation PEFCs with high durability. Recently, functional samples such as catalysts and batteries have been investigated by X-ray spectroscopy in two and three dimensions.[3b,c,f,j–m,4d,7] Nevertheless, there is limited information on the spatial arrangement and the mechanism for the Pt oxidation and dissolution in the Pt/C cathode catalyst layers.

In this study we designed and constructed the new high-performance XAFS beamline BL36XU at SPring-8 for spatially resolved XAFS measurements of PEFCs besides time-resolved XAFS measurements (Figure S1 in the Supporting Information).[7f,8] We succeeded in mapping Pt species in Pt/C cathode catalyst layers by a XAFS method and by a QXAFS method, and obtained spatial information on the site-preferential oxidation and leaching of Pt cathode nanoparticles in degraded PEFCs.

To measure the scanning XAFS and QXAFS spectra, we prepared two types of MEAs as typical examples: a) a MEA with a flat interface and few micro-cracks (denoted as MEA-A) and b) a MEA with micro-cracks (denoted as MEA-B). The detailed preparation is described in the Experimental Section of the Supporting Information. These MEAs were electrochemically aged by *I-V* load cycles and treated with accelerated durability tests (ADTs) by rectangle cycles

[*] Dr. S. Takao, Dr. O. Sekizawa, Dr. S. Nagamatsu, Dr. T. Kaneko, Dr. G. Samjeské, Dr. K. Higashi, Dr. K. Nagasawa, Prof. Dr. T. Uruga, Prof. Dr. Y. Iwasawa
Innovation Research Center for Fuel Cells
The University of Electro-Communications, Chofu
Tokyo 182-8585 (Japan)
E-mail: iwasawa@pc.uec.ac.jp
Dr. T. Yamamoto
Department of Mathematical and Material Sciences
The University of Tokushima, Minamijosanjima
Tokushima 770-8502 (Japan)
Dr. T. Tsuji, Dr. M. Suzuki, Dr. N. Kawamura, Dr. M. Mizumaki, Prof. Dr. T. Uruga
Japan Synchrotron Radiation Research Institute, SPring-8
Sayo, Hyogo 679-5198 (Japan)

[**] This work was supported by NEDO. XAFS measurements were performed with the approval of SPring-8 subject numbers 2010B1015, 2011A1031, 2011A1032, 2011B1039, 2011B1040, 2012A1024, 2012A1026, 2012B1024, 2013A7803, 2013B7803, and 2014A7806. XAFS = X-ray absorption fine structure.

Supporting information for this article is available on the WWW under http://dx.doi.org/10.1002/anie.201408845.

between 0.60–1.0 V vs. the reversible hydrogen electrode (RHE). We applied the ADT cycles to both MEA-A and MEA-B until the maximum power density decreased by 25% from those of the aging MEAs (Figures S2 and S3 and Tables S1 and S2). The Pt nanoparticles (2.5 nm) at the cathode grew to 8.5 nm on average by the ADT cycles (TEM images in Figure S4).

Sliced MEA samples for the XAFS measurements were prepared as follows. After the electrochemical procedures and ADT cycles, both anode and cathode gases were replaced by N_2 and the fuel cell was left until it reached an open circuit voltage (OCV) to prevent the sample from being exposed to high potentials. All procedures involving picking up the MEA from the PEFC stack, slicing the MEA to a 1 μm thick piece by an ultra-microtome, putting the sliced piece on a SiN membrane, arranging the sliced sample-membrane in a designed XAFS cell, and measuring XAFS spectra as shown in Figure 1 were performed in humid N_2 (see the Experimental Section in the Supporting Information). The resultant XAFS spectra are regarded to be equivalent to the XAFS spectra measured in situ after the aging and ADT cycles.

For the XAFS measurements, we used beams of 570×540 nm^2 and 228×225 nm^2, which are small enough compared to the in-between region of cathode-layer-edge/Pt-band and the micro-cracks in the cathode layer. We performed the scanning XAFS mapping experiments every 1 μm step in the 45×45 μm^2 or 125×95 μm^2 regions. We also carried out XAFS measurements by the QXAFS method. The acquisition time for the scanning XAFS and QXAFS measurements was 1.6 s or 15 minutes for each spectrum, respectively. We used the scanning XAFS for XANES analysis and the QXAFS for EXAFS analysis. The values at 11.600 keV were used as Pt L_{III}-edge jump values because the background in all XAFS spectra was very low. The Pt oxidation states in the cathode layer were estimated from a linear relationship between the Pt valence and the white line peak area (WLPA) of the normalized XANES spectra,[9] which we obtained using Pt foil, PtO, and PtO_2 as references.[4d,10] The qualities of the scanning XAFS and QXAFS spectra were high enough to allow mapping the Pt species in both MEAs (Figure 1 and Figure S5).

Figure 2 shows the (A,a,B,b: 570×540 nm^2 and D,E: 228×225 nm^2) Pt L_{III}-edge XANES mapping and (570×540 nm^2) QEXAFS analysis for MEA-A before (A–F) and after (a–c) the durability test; A and a: Pt quantity mapping, B and b: Pt valence mapping. Figure 2 corresponds to 2D depth mapping of the MEAs. During the aging of MEA-A the Pt valence mapping (B,E) in the whole observed cathode area did not show any significant change. The line profiles of the Pt quantity (blue) and Pt valence (red) along the red arrow of Figure 2B are shown in Figure 2C. The Pt valence is metallic in the whole region. In contrast, the distribution of the Pt quantity in MEA-A after the ADT cycles was heterogeneous as shown in Figure 2a. Interestingly, the Pt valence mapping (b) characterized the unique region between the cathode layer edge and the Pt band. The location of the Pt band with the high edge-jump intensity in the polymer electrolyte region coincides with the back scattering electron observation (Figure S6). The line profiles of the Pt quantity (blue) and Pt valence (red) along the red arrow of Figure 2b are shown in Figure 2c. The Pt species at positions a and b were metallic. The Pt valence in the cathode layer began to increase at a distance of roughly 3.2 μm from the cathode layer edge and showed a maximum (0.33 +) at positions d of c in the electrolyte membrane toward the Pt band (Figure 2c and also Figure S7). Thus, the Pt valence mapping shown in Figure 2b visualizes the existing area of oxidized Pt species in the degraded MEA-A. At the parts different from the boundary areas in the cathode layer no oxidized Pt species were observed. The resultant oxidized Pt species is produced first in the boundary of the cathode catalyst layer during the operating process involving repeated potential loads, while the Pt nanoparticles at the other parts of the cathode catalyst layer are metallic.

To characterize the structural parameters for the Pt species in the MEA-A sample, we performed the QEXAFS analysis for every 570×540 nm^2 area. The analyzed positions are indicated as a–c and a–d in Figure 2C and 2c, respectively, where d is a cathode/Pt band in-between the positions. The results of the analysis are shown in Figure 2F and summarized in the Figure 2G, where the Pt valences at each position are also shown. The overall QEXAFS Fourier transforms and curve-fittings for the MEA-A samples after the

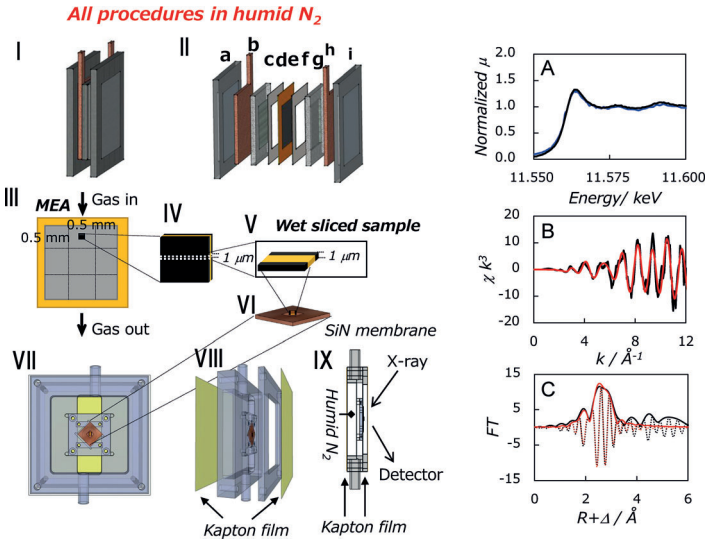

Figure 1. Preparation and arrangement of a sliced MEA piece on a SiN membrane and its mount in a XAFS cell for the XAFS measurements. I: a typical PEFC, II: its stacking structure (a: anode end plate; b: current collector; c: graphite plate; d: gasket; e: MEA; f: gasket; g: graphite plate; h: current collector; i: cathode end plate), III: place of the sample extracted, IV and V: dimension of the sample slicing, VI: mounting on a SiN membrane, VII: front view of the designed cell, VIII: side view of cell stacking, IX: directions of the X-ray irradiation and XAFS detector. A–C: typical XAFS data taken by the XAFS cell. A) Normalized XANES spectra for a cathode catalyst area in a degraded MEA-A by the XAFS mapping method (blue) and by the QXAFS method (black), B) the QEXAFS oscillation and its curve-fitting for the 570×540 nm^2 cathode area, C) the corresponding QEXAFS Fourier transform and its curve-fitting in R-space.

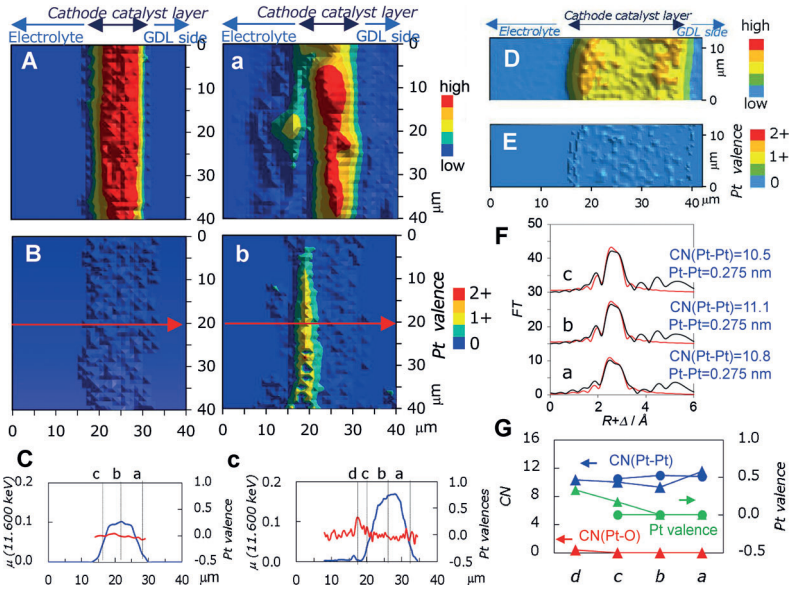

Figure 2. A,a) Pt L_{III}-edge jump mapping (Pt quantity mapping); B,b) Pt valence mapping, for MEA-A after the aging (A,B) and ADT cycles (a,b), respectively by the (570×540 nm) XAFS mapping method. C,c) Line profiles of the absorbance (μ) at 11.600 keV (blue) and Pt valence (red) in the scanning XANES spectra along the red arrows in (B) and (b), respectively. D,E) Pt L_{III}-edge jump mapping (Pt quantity mapping) and Pt valence mapping, respectively, for another MEA-A piece after the aging by the (228×225 nm^2) XAFS method. The quantity scale in (D) is not equivalent to that in (A). F) (570×540 nm^2) QEXAFS Fourier transforms (black) and curve-fittings (red) at positions a–c in (C). G) QEXAFS analysis by the curve-fittings (CN(Pt-Pt): blue, CN(Pt-O): red) and Pt valence (green) at the positions a–d in (C) and c for MEA-A before (circle) and after (triangle) the ADT cycles, respectively.

aging and ADT cycles are shown in Figures S8 and S9, respectively, and the determined structural parameters are listed in Tables S3 and S4. For the aging of MEA-A, the QEXAFS data at positions a–c in Figure 2C reveal only Pt–Pt bonds at 0.276 nm with coordination numbers (CNs) of 10.8 and no Pt–O bonds were observed, indicating the absence of oxidized Pt species in agreement with the Pt valence profile. On the other hand, the degraded MEA-A exhibited a CN of 0.6 for the Pt–O bond (0.206 nm) at positions d of c. The TEM observations revealed that many large metallic Pt particles (>15 nm) existed in these regions. Hence, the scanning XAFS areas inevitably involved both Pt nanoparticles (visible with TEM) and Pt ions/clusters (invisible with TEM; ×1500000). To estimate the concentration of the oxidized Pt species, we assumed: 1) a CN of 12 for the Pt^0 nanoparticles, 2) a 2+ valence for the oxidized Pt species as demonstrated by in situ XAFS,[4d,11] and 3) a CN(Pt-Pt) = 0 for the Pt^{2+} species in the electrolyte region between the cathode layer edge and Pt band. On this assumption, the Pt^0/Pt^{2+} ratio at positions d of c was calculated to be 7, which corresponds to 0.23+ of the Pt valence on average, and this valence fairly coincides with the Pt valence 0.33+ calculated from XANES mapping (Figure 2b). Further, we can estimate the CN of Pt–O for the Pt^{2+} species to be 4, which suggests that the high Pt oxidation species in the in-between region possesses a Pt^{2+}-O_4 coordination structure.

Figure 3 shows the Pt L_{III}-edge jump mapping (A), normalized WLPA mapping (B), and Pt valence mapping (C) around the Pt/C cathode layer with a micro-crack in the MEA-B after the ADT cycles. The micro-crack region was found to show much higher WLPA values than the other cathode areas. The Pt valence in most parts of the micro-crack region was calculated as 2+ by the linear relationship between the normalized WLPA and Pt valence,[4d,10] whereas Pt nanoparticles in the other cathode areas were zero valent (metallic) as shown in Figure 3C. This aspect is generally shown with other samples (Figure S10). The aging of MEA-B showed the metallic Pt^0 valence (not shown here) similar to the aging MEA-A in Figure 2B and 2E. Figure 3D shows the line-scan profiles of the Pt L_{III}-edge jump (Pt quantity) and Pt valence in the scanning XAFS spectra along the red arrow of Figure 3B. The Pt valence in the cathode catalyst layer began to increase from the positions with distances of roughly 1.2 and 2.4 μm (on both cathode sides of the micro-crack) far from the boundary edge to show the maximum Pt valence (Pt^{2+}) in the micro-crack area. No Pt nanoparticles/nanoclusters in the micro-crack region were observed by TEM (×1500000), whereas the presence of a small amount of Pt was indicated by energy dispersive spectroscopy (EDS). This means that there are only sub-nanosized species with less than five Pt atoms and/or Pt ions in the micro-crack region. Figure 3E shows the normalized QXANES spectra for the micro-crack areas 1, 5, and 6 of (B) and Pt and PtO as references. There existed an isosbestic point at 11569.7 eV in the QXANES spectra, which suggests the direct transformation of Pt^0 to Pt^{2+} species during the durability test. Figure 3F shows the QEXAFS Fourier transforms (black), curve-fittings (red), and determined structural parameters for areas 1–6 in the micro-crack region. The overall analysis of the structural parameters are shown in Figure S11 and Table S5. The micro-crack areas 1, 5, and 6 accommodated Pt^{2+} species (1.9–2.1+ valences) and the CN of Pt–O at 0.200 nm was 4.0 (±0.4) but no Pt–Pt bonding was observed. This means that the Pt^{2+} species does not have any Pt–Pt bonds but a Pt^{2+}-O_4 structure, such as the $[Pt(H_2O)_4]^{2+}$ ion. The water distribution inside the cathode may affect the oxidation event.[3c,f,m,7k,m,q,r] The presence of the Pt^{2+}-O_4 coordination species was also suggested with the degraded MEA-A in the region between the cathode layer edge and the Pt band. The Pt monomeric species $[Pt(H_2O)_4]^{2+}$ in aqueous solution is unstable, which is readily oxidized to Pt^{4+} and/or polymerized to PtO. There are Nafion ionomers with a sulfonic group in the micro-crack region as proved by EDS (F and S analysis) and the Pt^{2+} species may be stabilized by coordination with a sulfonic group (Nf-SO_3) to form $[Pt(Nf\text{-}SO_3)_x(H_2O)_y]^{2+}$. During the ADT cycles, Pt nanoparticles at the boundary of the Pt/C cathode layer toward the micro-crack are regarded to be first oxidized and then dissolved into the ionomers with moisture in the micro-crack region. As for the micro-crack areas 2–4 in Figure 3B,

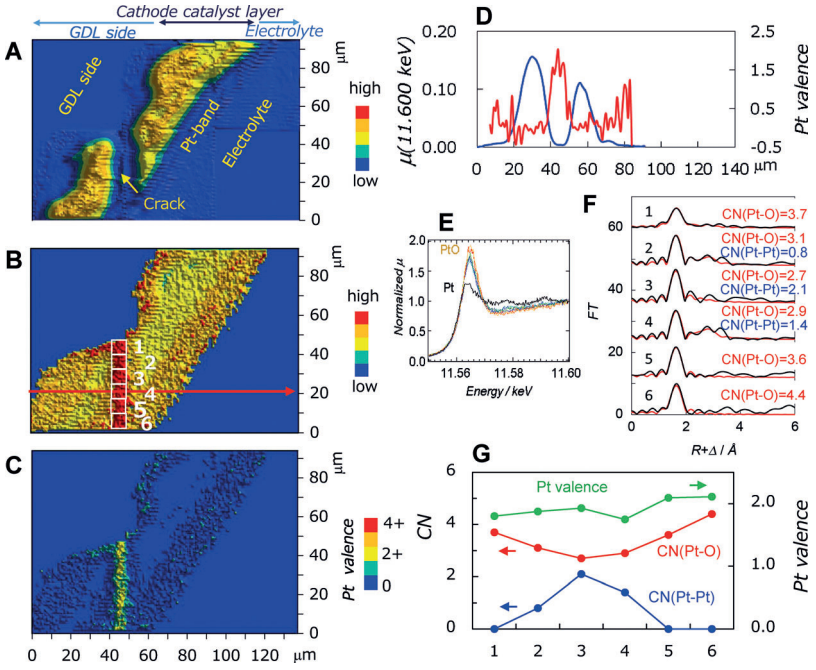

Figure 3. A) Pt L_{III}-edge jump mapping (Pt quantity mapping), B) normalized WLPA mapping, and C) Pt valence mapping for MEA-B after the ADT cycles by the XAFS mapping method. D) Line profiles of the absorbance (μ) at 11.600 keV (blue) and Pt valence (red) in the scanning XANES spectra along the red arrow in (B). E) Typical QXANES spectra of each micro-crack area in (B); crack 1: green, crack 5: blue, crack 6: red) and references (PtO and Pt). F) QEXAFS Fourier transforms (black) and curve-fittings (red) for micro-crack areas (1-6) in (B). G) QEXAFS analysis (CN(Pt-Pt): blue, CN(Pt-O): red), and Pt valence (green) for the micro-crack areas 1–6 in (B).

the CNs of Pt–Pt and Pt–O were 1.0 −1.8 and 2.7 −3.1, respectively, where the Pt valences are estimated as 1.8–1.9 +. These results indicate that mainly Pt^{2+} species are located in the micro-crack areas 2–4 and they may aggregate to $[(H_2O)_2Pt^{2+}(\mu\text{-}OH)]_n$ dimeric/cyclic species (the CNs of Pt–Pt for the dimer and cyclic hexamer are expected to be 1.0 and 1.7, respectively), but the Pt–Pt bonds were observed at a distance of 0.276 nm for metallic Pt species. Thus, it is more probable that both small Pt^0 clusters and Pt^{2+}-O_4 species coexist in the micro-crack areas 2–4.

The oxidized Pt species might have formed elsewhere in the cathode catalyst layer in the MEA-B and migrated toward the micro-crack during the ADT cycles, but this possibility may be excluded. The oxidized Pt species were located within the 1.2/2.4 μm range near the cathode layer edge with the maximum Pt valence (Pt^{2+}) in the micro-crack area. The Pt concentration in the micro-crack region was estimated by the edge-jump profile to be much lower than that in the flat part of the cathode catalyst layer, and the further degradation and dissolution should have been in progress during the ADT cycles. However, there were no Pt oxidized species in any areas inside the cathode layer far from the micro-crack, which indicates that the metallic Pt nanoparticles in parts of the cathode layer different from the 1.2/2.4 μm areas around the micro-crack were not oxidized to dissolve significantly by the ADT cycles. In separate experiments we have also analyzed the cathode catalyst layers of MEA pieces by the XAFS mapping method, and the obtained preliminary results demonstrate that there were only metallic Pt species around micro-cracks below 2 μm size and Pt^{2+} oxidized species were observed around micro-cracks larger than 2 μm. This site-preferential events were also observed in the cathode catalyst layer with the Pt band in the degraded MEA-A, where Pt nanoparticles are oxidized and leached within the 3.2 μm range near the boundary. Thus, the micro-cracks larger than 2 μm as well as the 3.2 μm boundary with the electrolyte are suggested to promote the MEA degradation by oxidizing and leaching Pt nanoparticles as Pt^{2+}-O_4 coordination species. These results on the degradation mechanism could be used to design MEA cathodes with better durability.

In conclusion the present XAFS study on MEAs reports the first success in mapping the Pt valence and identifying the major places for the oxidation and dissolution of Pt nanoparticles by the ADT cycles. The first spatial approaches to the Pt/C cathode catalysts in PEFCs by the XAFS mapping method and the QXAFS method gained new insights into the two-dimensional depth distribution of metallic and oxidized Pt species and the site-preferential mechanism for Pt oxidation and dissolution to form the Pt^{2+} monomeric species with a Pt-O_4 coordination structure in the degradation process. In situ XAFS experiments may provide further understanding of the MEA degradation mechanism by time-dependent mapping of a chemical change of Pt nanoparticles in the PEFC MEA under various conditions.

Experimental Section

In the XAFS method we scanned a MEA sample on a holder along a line against focused X-rays at a given X-ray energy, and then scanned the sample on the same line at the next given X-ray energy and repeated the line scan in the energy range every 0.4 and 2.0 eV, respectively, to obtain XANES and EXAFS spectra, and these procedures were repeated in the whole microscale area of the MEA Pt/C cathode layer. In the QXAFS method the MEA sample was fixed at a position during the measurement of a QXAFS spectrum, and then the focused beam was moved to the next point to measure the next QXAFS spectrum again. This procedure was repeated to obtain a QXAFS map in the target area. No beam damages in both XAFS methods were observed (Figures S12 and S13). The Pt L_{III}-edge XAFS spectra were measured in fluorescence mode at BL36XU and BL39XU. The X-ray beam (11.390–12.170 keV) was focused to $570 \times 540\ nm^2$ or $228 \times 225\ nm^2$ using a pair of elliptically bent KB mirrors (see the Experimental Section in the Supporting Information).

Received: September 5, 2014
Published online: October 22, 2014

Keywords: catalysts · electrochemistry · fuel cells · platinum · X-ray absorption spectroscopy

[1] a) G. Wu, K. L. More, C. M. Johnston, P. Zelenay, *Science* **2011**, *332*, 443; b) M. K. Debe, *Nature* **2012**, *486*, 43.

[2] C. Houchins, G. J. Kleen, J. S. Spendelow, J. Kopasz, D. Peterson, N. L. Garland, D. L. Ho, J. Marcinkoski, K. E. Martin, R. Tyler, D. C. Papageorgopoulos, *Membranes* **2012**, *2*, 855.

[3] a) M. B. Pomfret, J. C. Owrutsky, R. A. Walker, *Anal. Chem.* **2007**, *79*, 2367; b) K.-S. Choi, B.-G. Kim, K. Park, H.-M. Kim, *Fuel Cells* **2012**, *12*, 908; c) I. Manke, Ch. Hartnig, M. Gruenerbel, W. Lehnert, N. Kardjilov, A. Haibel, A. Hilger, J. Banhart, H. Riesemeier, *Appl. Phys. Lett.* **2007**, *90*, 174105; d) C. Rice, Y. Tong, E. Oldfield, A. Wieckowski, F. Hahn, F. Gloaguen, J.-M. Léger, C. Lamy, *J. Phys. Chem. B* **2000**, *104*, 5803; e) J. Healy, C. Hayden, T. Xie, K. Olson, R. Waldo, M. Brundage, H. Gasteiger, J. Abbott, *Fuel Cells* **2005**, *5*, 302; f) I. Manke, C. Hartnig, M. Grünerbel, J. Kaczerowski, W. Lehnert, N. Kardjilov, A. Hilger, J. Banhart, W. Treimer, M. Strobl, *Appl. Phys. Lett.* **2007**, *90*, 184101; g) D. Kramer, J. Zhang, R. Shimoi, E. Lehmann, A. Wokaun, K. Shinohara, G. Scherer, *Electrochim. Acta* **2005**, *50*, 2603; h) K. W. Feindel, L. P.-A. LaRocque, D. Starke, S. H. Bergens, R. E. Wasylishen, *J. Am. Chem. Soc.* **2004**, *126*, 11436; i) C. Lamy, S. Rousseau, E. M. Belgsir, C. Coutanceau, J.-M. Léger, *Electrochim. Acta* **2004**, *49*, 3901; j) J. P. Owejan, T. A. Trabold, D. L. Jacobson, M. Arif, S. G. Kandlikar, *Int. J. Hydrogen Energy* **2007**, *32*, 4489; k) T. A. Trabold, J. P. Owejan, D. L. Jacobson, M. Arif, P. R. Huffman, *Int. J. Heat Mass Transfer* **2006**, *49*, 4712; l) H. S. Casalongue, S. Kaya, V. Viswanathan, D. J. Miller, D. Friebel, H. A. Hansen, J. K. Nøskov, A. Nilsson, H. Ogasawara, *Nat. Commun.* **2013**, *4*, 1; m) T. Arlt, I. Manke, K. Wippermann, H. Riesemeier, J. Mergel, J. Banhart, *J. Power Sources* **2013**, *221*, 210.

[4] a) M. Tada, S. Murata, T. Asakoka, K. Hiroshima, K. Okumura, H. Tanida, T. Uruga, H. Nakanishi, S. Matsumoto, Y. Inada, M. Nomura, Y. Iwasawa, *Angew. Chem. Int. Ed.* **2007**, *46*, 4310; *Angew. Chem.* **2007**, *119*, 4388; b) N. Ishiguro, T. Saida, T. Uruga, S. Nagamatsu, O. Sekizawa, K. Nitta, T. Yamamoto, S. Ohkoshi, Y. Iwasawa, T. Yokoyama, M. Tada, *ACS Catal.* **2012**, *2*, 1319; c) N. Ishiguro, T. Saida, T. Uruga, O. Sekizawa, K. Nagasawa, K. Nitta, T. Yamamoto, S. Ohkoshi, T. Yokoyama, M. Tada, *Phys. Chem. Chem. Phys.* **2014**, DOI: 10.1039/c; d) S. Nagamatsu, T. Arai, M. Yamamoto, T. Ohkura, H. Oyanagi, T. Ishizaka, H. Kawanami, T. Uruga, M. Tada, Y. Iwasawa, *J. Phys. Chem. C* **2013**, *117*, 13094.

[5] T. Saida, O. Sekizawa, N. Ishiguro, M. Hoshino, K. Uesugi, T. Uruga, S. Ohkoshi, T. Yokoyama, M. Tada, *Angew. Chem. Int. Ed.* **2012**, *51*, 10311; *Angew. Chem.* **2012**, *124*, 10457.

[6] for examples; a) Y. Yu, H. Li, H. Wang, X. Z. Yuan, G. Wang, M. Pan, *J. Power Sources* **2012**, *205*, 10, and references in this review; b) S. F. Burlatsky, M. Gummalla, V. V. Atrazhev, D. V. Dmitriev, N. Y. Kuzminyh, N. S. Erikhman, *J. Electrochem. Soc.* **2011**, *158*, B322; c) W. Bi, G. E. Gray, T. F. Fuller, *Electrochem. Solid-State Lett.* **2007**, *10*, B101; d) J. Zhang, B. A. Litteer, W. Gu, H. Liu, H. A. Gasteiger, *J. Electrochem. Soc.* **2007**, *154*, B1005.

[7] a) I. L. C. Buurmans, B. M. Weckhuysen, *Nat. Chem.* **2012**, *4*, 873; b) E. De Smit, I. Swart, J. F. Creemer, G. H. Hoveling, M. K. Gilles, T. Tyliszczak, P. Kooyman, H. W. Zandbergen, C. Morin, B. M. Weckhuysen, F. M. F. De Groot, *Nature* **2008**, *456*, 222; c) I. D. Gonzalez-Jimenez, K. Cats, T. Davidian, M. Ruitenbeek, F. Meirer, Y. Liu, J. Nelson, J. C. Andrews, P. Pianetta, F. M. F. de Groot, B. M. Weckhuysen, *Angew. Chem. Int. Ed.* **2012**, *51*, 11986; *Angew. Chem.* **2012**, *124*, 12152; d) Y. C. K. Chen-Wiegart, W. M. Harris, J. J. Lombardo, W. K. S. Chiu, J. Wang, *Appl. Phys. Lett.* **2012**, *101*, 253901; e) N. Ishiguro, T. Uruga, O. Sekizawa, T. Tsuji, M. Suzuki, N. Kawamura, M. Mizumaki, K. Nitta, T. Yokoyama, M. Tada, *ChemPhysChem* **2014**, DOI: 10.1002/cphc.201400090; f) T. Tsuji, T. Uruga, K. Nitta, N. Kawamura, M. Mizumaki, M. Suzuki, O. Sekizawa, N. Ishiguro, M. Tada, H. Ohashi, H. Yamazaki, H. Yumoto, T. Koyama, Y. Senba, T. Takeuchi, Y. Terada, N. Nariyama, K. Takeshita, A. Fujiwara, S. Goto, M. Yamamoto, M. Takata, T. Ishikawa, *J. Phys. Conf. Ser.* **2013**, *430*, 012019; g) J. P. Owejan, T. A. Trabold, D. L. Jacobson, D. R. Baker, D. S. Hussey, M. Arif, *Int. J. Heat Mass Transfer* **2006**, *49*, 4721; h) M. Schumacher, I. Christl, A. C. Scheinost, C. Jacobsen, R. Kretzschmar, *Environ. Sci. Technol.* **2005**, *39*, 9094; i) B. Bozzini, L. D'Urzo, A. Gianoncelli, B. Kaulich, M. Prasciolu, I. Sgura, E. Tondo, M. Kiskinova, *J. Phys. Chem. C* **2009**, *113*, 9783; j) G. J. Nelson, W. M. Harris, J. J. Lombardo, J. R. Izzo, Jr., W. K. S. Chiu, P. Tanasini, M. Cantoni, J. Van herle, C. Comninellis, J. C. Andrews, Y. Liu, P. Pianetta, Y. S. Chu, *Electrochem. Commun.* **2011**, *13*, 586; k) T. Sasabe, S. Tsushima, S. Hirai, *Int. J. Hydrogen Energy* **2010**, *35*, 11119; l) A. Sakdinawat, D. Attwood, *Nat. Photonics* **2010**, *4*, 840; m) R. Flückiger, F. Marone, M. Stampanoni, A. Wokaun, F. N. Buechi, *Electrochim. Acta* **2011**, *56*, 2254; n) Y.-T. Chen, T.-N. Lo, Y. S. Chu, J. Yi, C.-J. Liu, J.-Y. Wang, C.-L. Wang, C.-W. Chiu, T.-E. Hua, Y. Hwu, Q. Shen, G.-C. Yin, K. S. Liang, H.-M. Lin, J. H. Je, G. Margaritondo, *Nanotechnology* **2008**, *19*, 395302; o) J. Vila-Comamala, Y. Pan, J. J. Lombardo, W. M. Harris, W. K. S. Chiu, C. David, Y. Wang, *J. Synchrotron Radiat.* **2012**, *19*, 705; p) V. Berejnov, Z. Martin, M. West, S. Kundu, D. Bessarabov, J. Stumper, D. Susac, A. P. Hitchcock, *Phys. Chem. Chem. Phys.* **2012**, *14*, 4835; q) H. Markötter, R. Alink, J. Haußmann, K. Dittmann, T. Arlt, F. Wieder, C. Tötzke, M. Klages, C. Reiter, H. Riesemeier, J. Scholta, D. Gerteisen, J. Banhart, I. Manke, *Int. J. Hydrogen Energy* **2012**, *37*, 7757; r) H. Markötter, J. Haußmann, R. Alink, C. Tötzke, T. Arlt, M. Klages, H. Riesemeier, J. Scholta, D. Gerteisen, J. Banhart, I. Manke, *Electrochem. Commun.* **2013**, *34*, 22.

[8] O. Sekizawa, T. Uruta, M. Tada, K. Nitta, K. Kato, H. Tanida, K. Takeshita, S. Takahashi, M. Sano, H. Aoyagi, A. Watanabe, N. Nariyama, H. Ohashi, H. Yumoto, T. Koyama, Y. Senba, T. Takeuchi, Y. Furukawa, T. Ohata, T. Matsushita, Y. Ishizawa, T. Kudo, H. Kimura, H. Yamazaki, T. Tanaka, T. Bizen, T. Seike, S. Goto, H. Ohno, M. Takata, H. Kitamura, T. Ishikawa, T. Yokoyama, Y. Iwasawa, *J. Phys. Conf. Ser.* **2013**, *430*, 012020.

[9] B. Ravel, M. Newville, *J. Synchrotron Radiat.* **2005**, *12*, 537.

[10] a) K. Nagasawa, S. Takao, K. Higashi, S. Nagamatsu, G. Samjeské, Y. Imaizumi, O. Sekizawa, T. Yamamoto, T. Uruga, Y. Iwasawa, *Phys. Chem. Chem. Phys.* **2014**, *16*, 10075; b) S. T. Christensen, J. W. Elam, F. A. Rabuffetti, Q. Ma, S. J. Weigand, B. Lee, S. Seifert, P. C. Stair, K. R. Poeppelmeiter, M. C. Hersam, M. J. Bedzyk, *Small* **2009**, *5*, 750.

[11] G. Samjeské, S. Nagamatsu, S. Takao, K. Nagasawa, Y. Imaizumi, O. Sekizawa, T. Yamamoto, Y. Uemura, T. Uruga, Y. Iwasawa, *Phys. Chem. Chem. Phys.* **2013**, *15*, 17208.